3D printing flexible Ga-doped ZnO films for wearable energy harvesting: thermoelectric and piezoelectric nanogenerators

Aicha S. Lemine[1,2], Jolly Bhadra[2,3,*], Kishor Kumar Sadasivuni[3], Anton Popelka[3], Swathi Yempally[3], Zubair Ahmad[2,3], Noora J. Al-Thani[2], and Anwarul Hasan[1,4,*]

[1] *Department of Mechanical and Industrial Engineering, College of Engineering, Qatar University, 2713 Doha, Qatar*

[2] *Young Scientists Center (QUYSC), Qatar University, Qatar University, 2713 Doha, Qatar*

[3] *Center for Advanced Materials (CAM), Qatar University, 2713 Doha, Qatar*

[4] *Biomedical Research Center (BRC), Qatar University, 2713 Doha, Qatar*

ABSTRACT

The 3D printing of energy harvesters using earth-abundant and non-toxic elements promotes energy sustainability and market competitiveness. The semiconducting behavior and non-centrosymmetric wurtzite crystal structure of gallium-doped zinc oxide (GZO) films make them attractive for thermoelectric and piezoelectric nanogenerators. This study investigates the thermal, structural, mechanical, thermoelectric, and piezoelectric properties of 3D-printed GZO nanocomposite films. Thermal analysis demonstrates the stability of the nanocomposite film up to 230 °C, making it suitable for wearable energy harvesters. The crystalline structure of the nanocomposite film aligns with the hexagonal wurtzite structure of ZnO and displays a bulk-like microstructure with a uniform distribution of elements. The presence of Ga 2p, Zn 2p, O 1 s, and C 1 s core levels confirms the development of the nanocomposite film, characterized by a fine granular structure and a conductive domain compared to the neat resin film. The inclusion of GZO nanofillers tailors the stress–strain behavior of the nanocomposite film, enhancing flexibility. The 3D-printed GZO nanocomposite films demonstrate a promising thermoelectric power factor and piezoelectric power densities, along with mechanical flexibility and thermal stability. These advancements hold significant potential for wearable and hybrid energy generation technologies.

1 Introduction

Wearable electronic devices have seen rapid advancements in flexibility, integration, and intelligence, driven by flexible electronics, big data, and artificial intelligence technologies [1]. These developments expand applications in health monitoring, human–machine interaction, and the Internet of Things [1]. However, energy supply remains a major challenge for these devices, especially given the need for

Address correspondence to E-mail: jollybhadra@qu.edu.qa; ahasan@qu.edu.qa

Springer

flexibility and integration [2]. Most wearable devices currently rely on replaceable batteries, which are rigid, have limited lifetimes, and pose potential environmental risks, conflicting with sustainable energy goals such as promoting renewable energy and reducing environmental pollution [3].

Self-powered technology, which allows devices to harvest energy from their environment, offers a promising solution for the sustainable energy supply of wearable systems [4]. Wearable devices can harvest energy from various sources, including thermal, mechanical, and chemical energy [5]. Significant efforts have been made to enhance energy harvesting systems, with particular attention to thermoelectric (TE) and piezoelectric (PE) energy harvesters [6–8]. Wearable thermoelectric generators convert the body's thermal energy into electrical energy, while piezoelectric generators convert mechanical deformations into electrical energy [9, 10]. Hybrid energy harvesters, which combine multiple energy sources, further improve efficiency and reliability, making wearable devices self-sustaining and battery-free [11].

Conventional techniques for developing wearable energy harvesters face design limitations, which can be overcome by 3D printing technology [12]. 3D printing, an additive manufacturing process, creates three-dimensional parts layer by layer using computer-aided design (CAD) [13]. It offers advantages over traditional manufacturing processes, including rapid prototyping, flexible design, strong and lightweight features, minimal waste, cost-effectiveness, ease of access, and environmental benefits [14, 15]. Liquid Crystal Display (LCD) printing, a popular 3D printing method, uses ultraviolet (UV) light-emitting diodes (LEDs) to cure a photocurable liquid resin, offering fast print speeds and high-quality finishes [16, 17]. Kim et al. developed 3D-printed thermoelectric films using Bismuth Telluride (Bi_2Te_3) in 300μm thickness to perfectly fit wearable heat sources [18]. He et al. prepared 3D-printed composites of photoresin and Bismuth Antimony Telluride ($Bi_{0.5}Sb_{1.5}Te_3$) with good thermoelectric and mechanical properties [19]. Park et al. enhanced the performance of thermoelectric composites using a photocured resin matrix and Silver Selenide (Ag_2Se) fillers for energy harvesting [20]. Zhou et al. designed 3D-printed piezoelectric nanogenerators using Barium Titanate ($BaTiO_3$) nanoparticles and Poly(vinylidene fluoride-co-trifluoroethylene) (P(VDF-TrFE)) for stretchable energy harvesting [21]. Kim et al. created high-performance 3D printable

piezoelectric composites using $BaTiO_3$ nanoparticles within a photocurable resin matrix [22].

Using earth-abundant materials for 3D printing energy harvesters can reduce manufacturing costs and increase market competitiveness [23]. Zinc Oxide (ZnO) is a promising, inexpensive, and abundant material with high stability and non-toxic properties, making it suitable for wearable thermoelectric and piezoelectric applications [24]. ZnO, a wide bandgap semiconductor with a non-centrosymmetric wurtzite crystal structure, can be doped with Gallium (Ga) to improve electrical conductivity and modify crystal structure, enhancing energy conversion efficiency compared to undoped ZnO films [25, 26]. Pandiyarasan et al. used the solvothermal method to grow nanostructured ZnO on fabrics for wearable thermoelectric generators [27]. Mahapatra et al. developed flexible piezoelectric nanogenerators based on ZnO:PVDF composite using the hydrothermal method for vibrational energy harvesting and wearable shoe insole pedometer applications [28].

While extensive research has been conducted on the structure and energy harvesting capabilities of ZnO films for wearable thermoelectric and piezoelectric applications, there is a notable gap in integrating 3D printing technology for developing flexible ZnO films suitable for these applications [27, 29]. This study aims to address this gap by investigating the use of 3D printing technology to fabricate flexible films composed of earth-abundant and non-toxic elements, specifically Ga-doped ZnO (GZO), for thermoelectric and piezoelectric energy harvesting applications to promote energy sustainability. The research employs 3D printing to produce flexible nanocomposite films using photocurable resin and GZO nanofillers to enhance their thermoelectric and piezoelectric properties, as depicted in Fig. 1. Various measurements, including thermal, structural, mechanical, thermoelectric, and piezoelectric analyses, were performed on the 3D-printed films to assess their energy harvesting capabilities.

2 Experimental

2.1 Materials

GZO nanopowder was supplied by Nanochemazone with 99% purity and an average particle size of 50–60 nm. Photocurable LCD-C resin was provided by
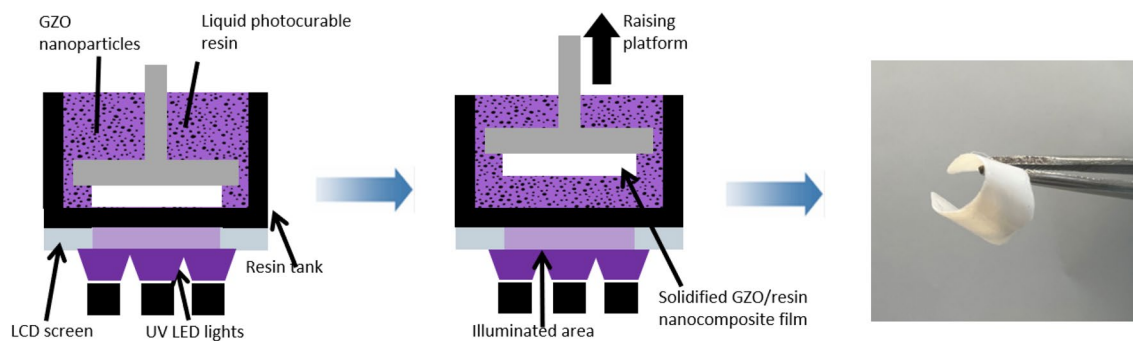
Fig. 1 Schematic illustration of 3D printing for a photocurable resin-GZO nanocomposite film using an LCD resin printer

SparkMaker with a liquid density of 1.10 g/mL and UV curing at 355–420 nm.

2.2 Methods

GZO nanopowder was added to the photocurable LCD-C resin in equivalent weight fractions, followed by overnight magnetic stirring at room temperature (25 °C) for homogenization. CHITUBOX slicing software was used to slice a 3D CAD model into thin layers for printing, with parameters such as an exposure time of 120 s and a lift speed of 60mm/min adjusted accordingly. The Phrozen Sonic Mini Resin 3D Printer was employed to print the photocurable resin-GZO nanocomposite, using a layer height of 50 μm through photopolymerization on an LCD screen. This process utilized a 405 nm photocuring wavelength provided by an array of LEDs, which uniformly distributed UV light over the print area. Subsequently, the 3D-printed films of photocurable resin and photocurable resin-GZO nanocomposite were immediately submerged in isopropyl alcohol (IPA) to remove any residual uncured resin before being left to dry at room temperature, ensuring a clean and smooth surface finish.

2.3 Characterizations

2.3.1 Thermal stability

The thermal stability of 3D-printed photocurable resin and photocurable resin-GZO nanocomposite films was assessed using Thermogravimetric Analysis (TGA 4000, PerkinElmer, USA). The analysis was conducted from room temperature to 800 °C at a constant heating rate of 10 °C/min in an inert nitrogen (N_2) atmosphere.

2.3.2 Structure and morphology

X-ray diffractometer (XRD; PANalytical EMPYREAN, UK) with a CuKα radiation source ($\lambda = 1.54$Å) was used to identify phases and determine grain sizes of the printed resin and nanocomposite films. Field emission scanning electron microscopy (FE-SEM; FEI Nova Nano-SEM 450, USA), coupled with energy-dispersive X-ray spectroscopy (EDS), examined the surface morphology and elemental distribution of the printed films. Chemical bonding analysis was conducted on the printed films using X-ray photoelectron spectroscopy (XPS; Kratos AXIS Ultra DLD, USA). Surface topography and electrical characteristics were analyzed using conductive atomic force microscopy (C-AFM; Asylum Research MFP-3D, USA) with an ORCA probe.

2.3.3 Mechanical properties

The Young's Modulus, tensile strength, and ductility of the printed resin and nanocomposite films were evaluated using a universal testing instrument (Lloyd LS 1K Plus, UK) following ASTM D882 standards, with a constant engineering strain rate of 5mm/min.

2.3.4 Thermoelectric properties

The electrical conductivities of the printed resin and nanocomposite films were calculated from C-AFM measurements. The Seebeck coefficients of the printed films were measured using the experimental setup developed by Hasan et al. [30]. This setup consisted of an infrared thermometer (RayTemp 8, UK), a hot

plate, and a source measure unit instrument (SMU; Keithley 2400, USA). Both ends of the films were coated with conductive silver paste (Sigma-Aldrich) to serve as electrodes. A hot plate was used to heat one side of the film and create a temperature gradient (ΔT), generating a thermoelectric voltage (ΔV) measured by the SMU instrument. The slope technique was then employed to determine the Seebeck coefficient ($S = \Delta V/\Delta T$) values from the generated thermoelectric voltage as a function of the temperature gradient on both photocurable resin and photocurable resin-GZO nanocomposite films.

2.3.5 Piezoelectric properties

The piezoelectric output voltages of the printed resin and nanocomposite photocurable films were measured using the experimental setup developed by Parangusan et al. [31]. The setup included a dynamic signal acquisition module (National Instrument, NI USB-4431, USA) and interactive output measurement software. Conductive silver paste was applied to both the top and bottom surfaces of the printed films, serving as electrodes. These silver-pasted surfaces were then connected to electrical wires using conductive copper tape to facilitate connection with the dynamic signal acquisition module. Various mechanical deformation modes, such as tapping and bending, were applied to the films to measure the output piezoelectric voltage using the interactive output measurement software.

3 Results and discussions

3.1 Thermal stability

TGA analysis examines the thermal stability of GZO nanopowder and 3D-printed films made from photocurable resin and photocurable resin-GZO nanocomposite, as shown in Fig. 2. The TGA curve for GZO nanopowder demonstrated consistent thermal stability from room temperature to 800 °C without decomposition, a characteristic often associated with ZnO nanoparticles due to their strong interatomic bonds from the electropositive nature of metal oxides [32, 33]. Figure 2a, b shows the weight loss and weight loss rate curves for neat resin and nanocomposite films, indicating stability from 25 °C to around 230 °C, suitable for wearable energy harvesters, especially thermoelectric and piezoelectric nanogenerators [1]. Beyond 230 °C, a sudden decline in weight suggests thermal decomposition [34].

The addition of GZO nanoparticles significantly affected the thermal degradation of neat photocurable resin, resulting in a 50% weight residue for the nanocomposite, primarily due to the presence of GZO nanoparticles. This confirms an equal weight ratio of GZO nanofillers and the photocurable resin matrix in the nanocomposite film. This equal weight ratio facilitated the creation of a suitable nanocomposite slurry for 3D printing, ensuring UV light penetration without hindrance and preventing printing failure
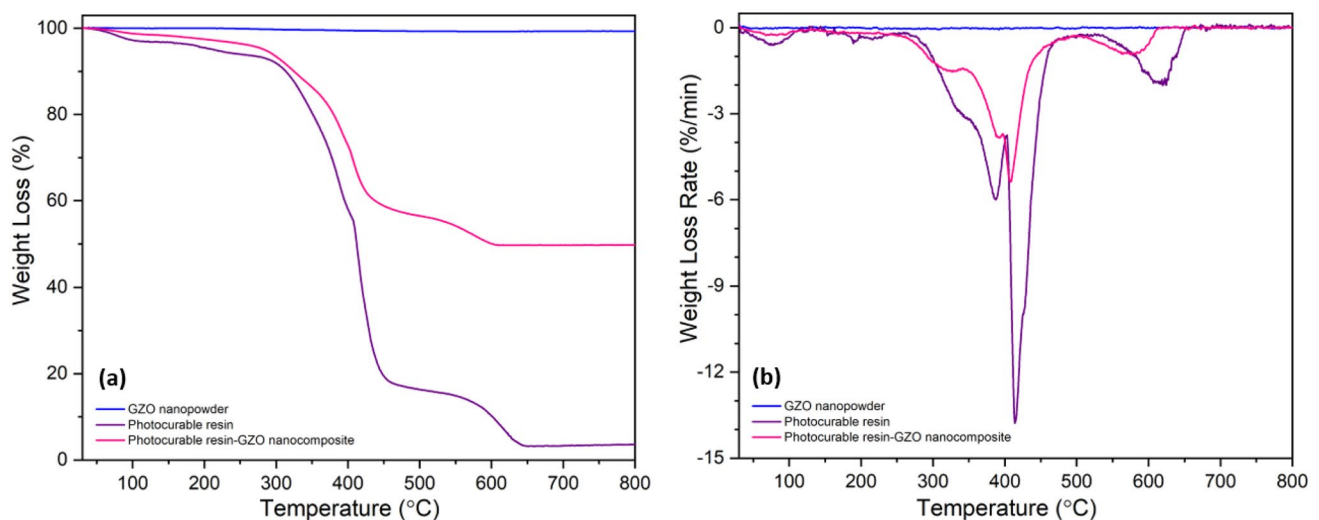

Fig. 2 TGA curves of **a** weight loss and **b** weight loss rate for GZO nanopowder, photocurable resin, and photocurable resin-GZO nanocomposite

[35]. Previous research by Zhao et al. highlighted the importance of liquid precursor transparency in enhancing UV light permeability and achieving uniform photo-crosslinking [36]. Although the decomposition temperature slightly shifted, the most significant change was in the weight loss rate, which decreased from − 13.7%/min to − 5.30%/min for resin and nanocomposite films, respectively, as shown in Fig. 2b. This decrease can be attributed to the uniform dispersion of nano-sized GZO particles, which enhance thermal stability by strengthening the interfaces between the matrix and filler, leading to uniform thermal distribution and decomposition within the resin-GZO nanocomposite [36].

3.2 Structure and morphology

The XRD analysis investigates the phases and grain sizes in the photocurable films. Figure 3 illustrates the diffraction profile of GZO nanopowder, characterized by distinct, sharp, and narrow diffraction peaks, indicating a crystalline phase [37]. In contrast, the XRD profile of the neat photocurable resin displays an amorphous phase with a broad diffraction peak [38]. Moreover, the diffraction pattern of the photocurable resin-GZO nanocomposite reveals crystalline diffraction peaks consistent with GZO nanopowder, aligning with the peaks of ZnO hexagonal wurtzite structure (JCPDS: 36-1451) [39]. The fundamental peak of GZO nanopowder and the

Fig. 3 XRD patterns of GZO nanopowder, photocurable resin, and photocurable resin-GZO nanocomposite

photocurable nanocomposite film is observed at a low Bragg's angle (2θ) of 36.4°, exhibiting strong intensity and an indexed crystal plane of (101). The preferred orientation of GZO nanoparticles is observed in the [101] direction along the c-axis, corresponding to the XRD peak with the highest intensity [40].

Figure 3 demonstrates agreement in intensity for the crystalline diffraction peaks of GZO nanofiller and photocurable resin-GZO nanocomposite, particularly at (010), (002), and (101) planes. A slight positional shift in diffraction peaks of the photocurable nanocomposite from the nanofiller nanopowder is observed, possibly caused by mismatched crystalline structures and the formation of heterojunctions between the two phases in the nanocomposite [37]. Integral breadth analysis on the XRD patterns, using the Warren–Averbach method through Eq. (1), determines the average grain size and residual lattice strains of GZO nanopowder, photocurable resin, and photocurable resin-GZO nanocomposite [41].

$$\frac{\beta_{hkl}^2}{\tan^2\theta} = \frac{1}{D}\left(\frac{\beta_{hkl}}{\tan\theta\sin\theta}\right) + 25(\varepsilon^2), \qquad (1)$$

where β_{hkl} is the width of the peak (hkl) at half-maximum intensity in radians, λ is the wavelength of the x-ray beam, θ is the diffraction angle of the peak position in radians, D is the average grains size, and ε is the lattice strain [41]. Fitting the data of $\beta_{hkl}^2/\tan^2\theta$ vs. $\beta_{hkl}/(\tan\theta\sin\theta)$ through the Gaussian function yielded the best linear regression fit of approximately 0.94 for all recognized diffraction peaks in XRD patterns.

Table 1 presents the average grain size of 25nm for the GZO nanopowder and 22nm for the photocurable resin-GZO nanocomposite film. The decrease in grain size of the nanocomposite is attributed to the reduced clustering of GZO nanoparticles, hindered by interactions with polymeric chains from the resin matrix [42]. This hindering effect potentially promotes the effective dispersion of GZO nanoparticles within the resin matrix, enhancing interfacial adhesion and overall interphase properties of the photocurable nanocomposite [43]. Residual lattice strains increase from 0.089% to 0.341% for GZO nanopowder and photocurable resin-GZO nanocomposite, respectively. This increase may result from microscopic strains developed due to the dispersion of GZO nanoparticles in the resin matrix, inducing local structural distortions, particularly at nanofiller and matrix interphases [24].
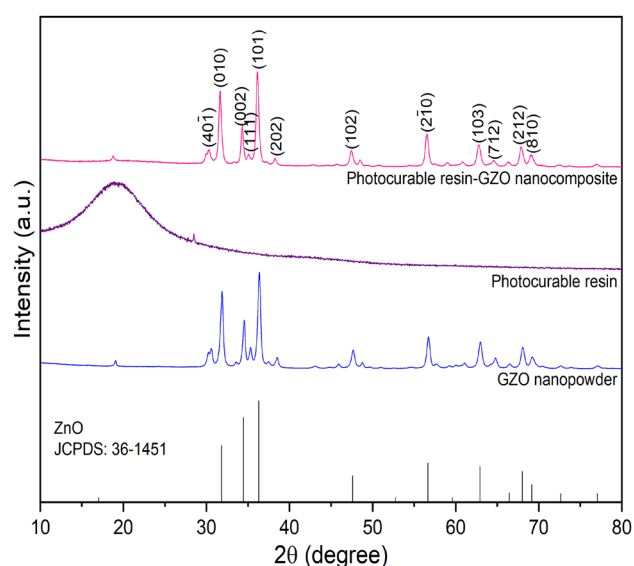
Table 1 XRD analysis of crystallite size (D), microscopic lattice strain (ε), lattice parameters (a and c), and volume of the unit cell (V)

Sample	D (nm)	ε (%)	a (Å)	c (Å)	a/c	V (Å³)
GZO nanopowder	25	0.0890	3.25	5.20	0.624	47.5
Photocurable resin	–	–	–	–	–	–
Photocurable resin-GZO nanocomposite	22	0.341	3.25	5.21	0.624	47.6

The crystallographic parameters of the photocurable nanocomposite film and GZO nanopowder, including lattice constants (a, b, and c), can be calculated using the crystallographic plane indices (h, k, and l) as follows [44]:

$$d_{(hkl)} = \left[\frac{4}{3}\left(\frac{h^2 + k^2 + hk}{a^2}\right)\right]_0^{-0.5}, \tag{2}$$

where $d_{(hkl)}$ is the inter-planar spacing derived from Bragg's law and XRD patterns [44]. The lattice parameters of the standard reference ZnO are $a_o = b_o = 3.25$Å and $c_o = 5.21$Å [39]. Table 1 demonstrates the alignment of lattice parameters and the ratio (a/c) between the photocurable resin-GZO nanocomposite, GZO nanopowder, and the standard reference (JCPDS: 36-1451) [39]. This confirms the phase purity and crystallinity of the developed nanocomposite film, which is consistent with the observed XRD profiles. However, the slight deviation in the c-lattice constant for the nanocomposite film may result in unit cell elongation along the c-axis, potentially leading to alterations in the volume (V) of the unit cell, calculated as follows [45]:

$$V = \frac{\sqrt{3}}{2}a^2c. \tag{3}$$

The unit cell volumes of GZO nanopowder and the nanocomposite film are 47.5Å³ and 47.6Å³, respectively, compared to bulk ZnO at 47.5Å³, as displayed in Table 1 [44]. These minor changes in unit cell volume could be attributed to the evolution of the nanocomposite microstructure, potentially resulting in distortions exerted by polymer chains from the resin matrix on GZO nanofillers [46].

SEM analysis, coupled with EDS, is utilized to investigate the surface morphology and elemental distribution of the photocurable resin and the photocurable resin-GZO nanocomposite films, as depicted in Fig. 4a, b. The FE-SEM image of the neat resin film reveals a smooth surface with evenly distributed C and O elements, identified by EDS peaks at 0.28 keV and 0.51 keV, respectively. In contrast, the FE-SEM image of the nanocomposite film demonstrates the incorporation of GZO nanoparticles within the resin matrix without significant voids or cracks. The microstructure evolution of 3D-printed nanocomposite films through a short and immediate UV curing process might result in a bulk-like and low-defect
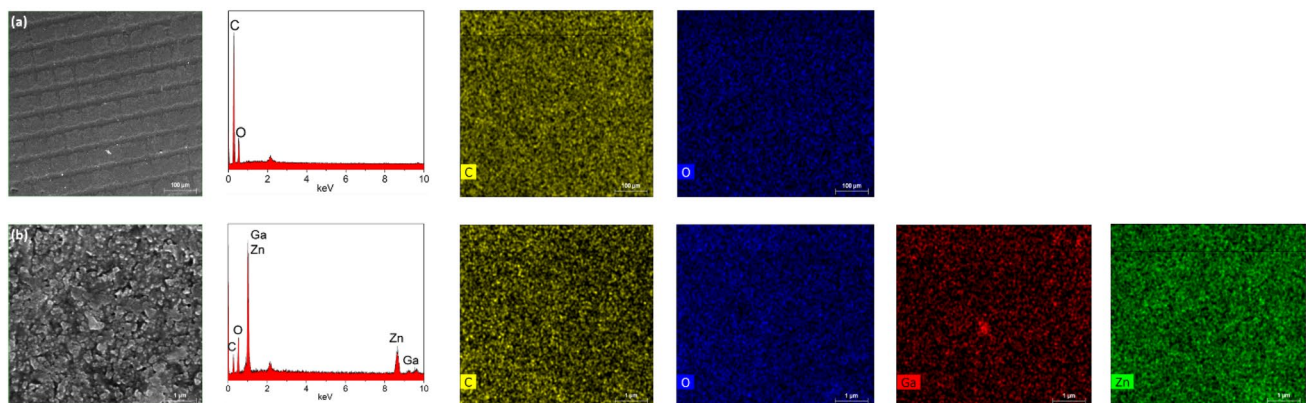

Fig. 4 FE-SEM images, EDS spectra, and elemental mapping analysis of **a** photocurable resin and **b** photocurable resin-GZO nanocomposite films
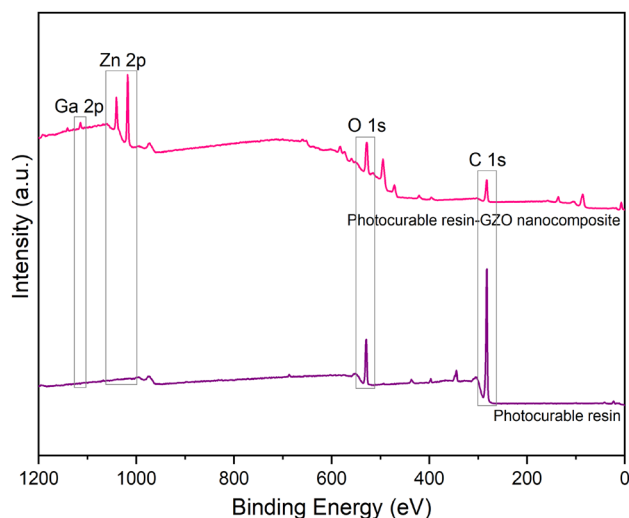
Table 2 SEM–EDS analysis of photocurable resin and photocurable resin-GZO nanocomposite films

Sample	Element (wt%)			
	Ga	Zn	O	C
Photocurable resin	–	–	33.8	66.2
Photocurable resin-GZO nanocomposite	6.06	46.3	23.3	24.3

Fig. 5 Full-survey XPS spectra of photocurable resin and photocurable resin-GZO nanocomposite films

microstructure. This improvement could enhance the mechanical, thermoelectric, and piezoelectric properties of the nanocomposite [35]. The UV curing process, when applied with appropriate UV light intensity and exposure time, may eliminate the necessity for subsequent annealing processes to enhance the density of the printed films [35].

Elemental mapping analysis of the photocurable nanocomposite film illustrates a uniform distribution of Ga, Zn, and O elements originating from the GZO nanofillers within the photocurable resin matrix. Table 2 summarizes the EDS analysis conducted on the FE-SEM images of the photocurable resin and the photocurable resin-GZO nanocomposite films. The EDS data of the neat resin film predominantly consist of C and O elements, with weight compositions of 66wt% and 34wt%, respectively. In contrast, the photocurable film of the resin-GZO nanocomposite displays the highest weight composition of Zn element at 46wt%, followed by C and O elements, each comprising nearly equivalent compositions of 24wt% and 23wt%, respectively. Additionally, the n-type dopant, Ga element, constitutes 6wt% of the nanocomposite film. Notably, the Ga and Zn content in the nanocomposite film does not exhibit a Ga/Zn ratio close to two, suggesting the absence of a Zinc Gallate ($ZnGa_2O_4$) spinel compound, which aligns with the phase purity observations from the XRD analysis.

XPS analysis examined the chemical bonding of the photocurable resin and its composite with GZO nanoparticles. In Fig. 5, the full-range XPS spectra revealed distinctive core levels, including Ga 2p, Zn 2p, O 1s, and C 1s, indicating the composition of the nanocomposite film. Conversely, the neat resin film exhibited only peaks corresponding to C 1s and O 1s. This combination of core levels in the nanocomposite film suggests its formation from multiphase constituents compared to the neat resin film, supported by XRD and SEM–EDS analyses [47]. Gaussian spectral fitting of XPS data further elucidated the binding

states of the elements in the samples [48]. Figure 6a, b illustrates the resolution of the C 1s peak into two peaks, C–O–C and H–C/C–C, for both neat resin and nanocomposite films, with negligible differences in binding energies. Figure 6c, d shows the resolution of the O 1s peak into peaks of H–O/C–O and Zn–O for the nanocomposite film, while the resin film exhibited only an H–O/C–O peak.

Following the variations in the peak intensities of O 1s, it is observable that Zn–O is the dominant chemical bond in the nanocomposite film. The variations in the peak positions of Zn–O and H–O/C–O in nanocomposite film could be attributed to a dipole moment at the interface between GZO nanofillers and the resin matrix [16]. This indicates strong chemical interactions caused by charge transfer developed during the photopolymerization process of the 3D-printed nanocomposite film [16]. As a result, the printed nanocomposite is distinguishable from a simple physical mixture due to extensive chemical interactions among its constituents, including interfacial bonds and interdiffusion regions [43]. Figure 6e, f illustrates the XPS spectra of the Zn 2p core level, revealing peaks attributed to the Zn–O–Ga bond and spin–orbit splitting of Zn $2p_{1/2}$ and Zn $2p_{3/2}$ for the nanocomposite film. Similarly, Fig. 6g, h shows the resolution of the Ga 2p peak into peaks of Ga $2p_{3/2}$ and Ga–O for the nanocomposite film.

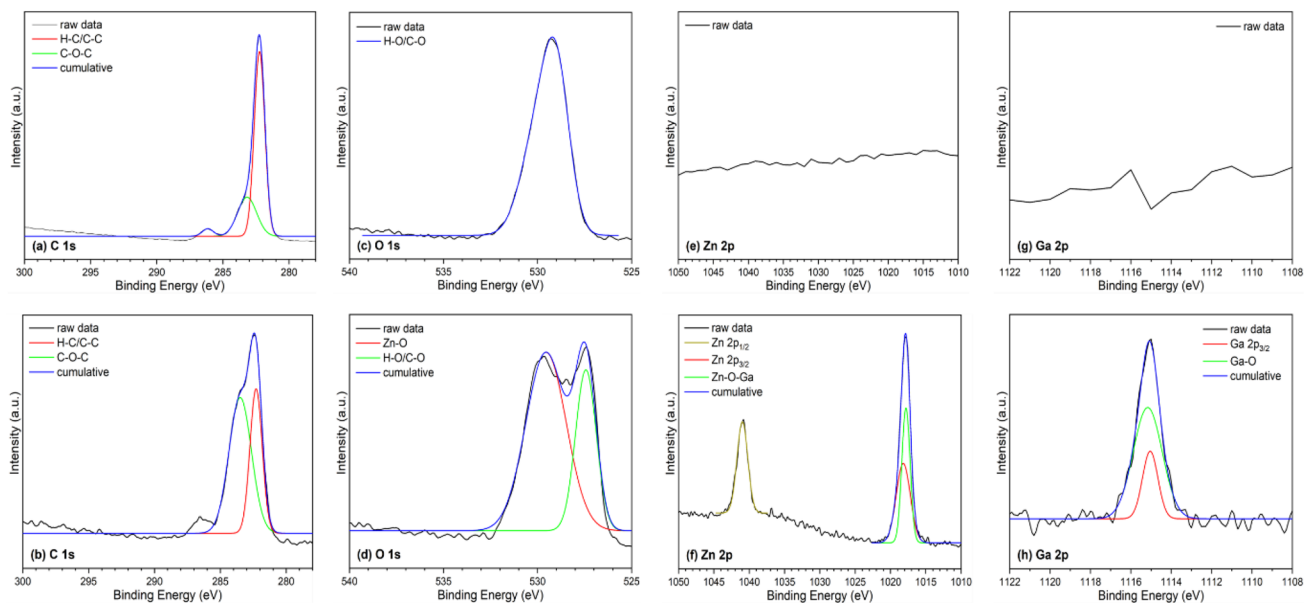C-AFM was utilized to analyze the film topography and electrical characteristics of the 3D-printed

Fig. 6 XPS spectra of **a**, **b** C 1s, **c**, **d** O 1s, **e**, **f** Zn 2p, and **g, h** Ga 2p core levels for photocurable resin (top row) and photocurable resin-GZO nanocomposite (bottom row) films

Fig. 7 C-AFM surface topography (top row) and current mapping (bottom rows) images of 3D-printed **a**, **b** photocurable resin and **c**, **d** photocurable resin-GZO nanocomposite films. All measurements were obtained from a $5 \times 5 \mu m^2$ surface area at a bias voltage of 10V
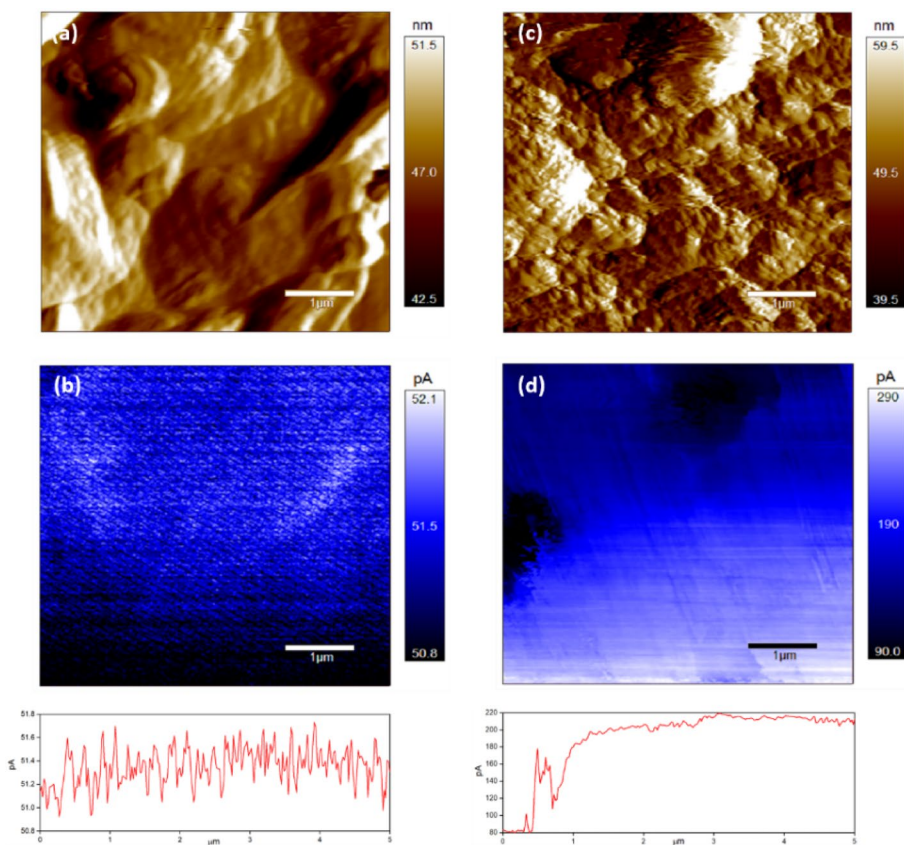
films. Figure 7a, c depicts the topography images, revealing that the photocurable nanocomposite film exhibits a fine granular structure compared to the neat film, suggesting the presence of multiple nano-sized GZO particles dispersed in the resin matrix [41]. Weak phase separation between the GZO

nanofillers and resin matrix is also observed, resulting in a more homogeneous and non-porous structure, which could promote strong interfacial bonds and enhance properties. Additionally, the increase in surface roughness values from 114 to 262nm for neat and nanocomposite films, respectively, indicates the formation of a multi-component heterogeneous nanocomposite. The increased nanoscale surface roughness of the nanocomposite film may significantly contribute to the enhancement of output power in flexible energy harvesters [5]. Ji et al. reported on surface roughness modifications to improve the output voltage of the piezoelectric layer due to increased contact surface area [49].

Figure 7b, d displays the current mapping image and line profile of the photocurable resin and nanocomposite films, revealing a uniform conductivity domain of 200 pA for the nanocomposite film. This conductive domain exhibits high carrier delocalization, possibly attributed to the crystalline structure of the nanocomposite film, as indicated by its XRD profile, leading to enhancements in the mobility of charge carriers [50]. This finding aligns with SEM observations of homogeneous elemental distribution and XPS results indicating the presence of charge transfer interactions resulting from strong interfacial bonds between GZO-reinforced nanoparticles and the resin matrix. Consequently, the electrical current flows along the network established from various heterojunctions between the matrix phase and conductive GZO nanofillers [50]. The in-situ photo-crosslinking of the 3D-printed nanocomposite film may also contribute to the uniform degree of crosslinked networks reinforced with GZO nanoparticles achieved at ambient temperature within seconds to minutes [36]. Photo-crosslinking offers advantages in eliminating both post-polymerization modifications to facilitate charge mobility and possible side reactions encountered with thermal-crosslinking at high temperatures [36].

3.3 Mechanical properties

The Young's Modulus, tensile strength, and ductility of 3D-printed resin and nanocomposite films were assessed using a universal testing instrument following ASTM D882 standards. Young's modulus, measuring a material's resistance to stretching or deformation under an applied load, was significantly lower in the nanocomposite film (85 MPa) compared to the

Table 3 Mechanical properties of 3D-printed films at room temperature

Sample	Young's Modulus (MPa)	Tensile strength (MPa)	Ductility (%)
Photocurable resin	174.3	13.4	73.7
Photocurable resin-GZO nanocomposite	85.03	4.07	39.3

neat resin film (174 MPa), as shown in Table 3 [41]. This indicates that the nanocomposite film offers higher flexibility and is more easily deformed, which is desirable for applications in wearable energy harvesters [51]. GZO nanofillers appear to modify the stress–strain behavior, enhancing the flexibility of the nanocomposite film and allowing it to bend, flex, or deform to a greater extent before failure [51]. The resin film is composed purely of polymer chains, resulting in a higher density of photo-crosslinked networks, which would increase resistance to elastic deformation [52]. The tensile strength, crucial for the safety and reliability of wearable energy harvesters, represents the maximum stress a material can withstand, while being stretched or pulled before breaking [26]. The nanocomposite film exhibited a tensile strength of 4 MPa compared to 13 MPa for the neat resin film, as indicated in Table 3.

The presence of GZO nanofillers could potentially increase the spacing between the polymer chains of the resin matrix, leading to a reduction in the tensile strength of the nanocomposite film and an increase in its flexibility [43]. Energy harvesters with ductility offer increased flexibility and deformability without rupturing, enhancing user comfort in wearable applications [53]. As shown in Table 3, the nanocomposite film demonstrates a ductility of 39%, whereas the neat resin film exhibits a higher ductility of 73%. The strong interfacial bonds between GZO-reinforced nanoparticles and the resin matrix in the nanocomposite film may restrict the mobility of polymer chains, resulting in reduced ductility compared to the neat resin film [53]. Nevertheless, the ductility of the 3D-printed photocurable resin-GZO nanocomposite film remains adequate and surpasses that of drop-casted Fe-ZnO/PVDF nanocomposite films developed for flexible piezoelectric energy harvesters [54]. The mechanical flexibility of the GZO-resin nanocomposite film enables better integration of thermoelectric energy harvesters

onto curved surfaces for applications in body heat-powered wearable energy devices [55].

3.4 Thermoelectric properties

For optimal thermoelectric performance, the 3D-printed films must demonstrate enhanced electrical conductivity and Seebeck coefficient [56]. The nanocomposite film exhibits a superior electrical conductivity of 4001 nS/m at room temperature compared to the neat resin film, as shown in Table 4. Additionally, the improved structure and morphology of the nanocomposite film, as revealed by XRD, SEM, and AFM analyses, can potentially decrease carrier collisions and enhance current flow [57]. The negative Seebeck coefficient value for the nanocomposite film, as depicted in Table 4, indicates that electrons are the primary charge carriers, owing to the n-type conductivity of GZO nanofillers [57]. The Seebeck coefficient, or thermopower, measures the induced thermoelectric voltage in response to a temperature gradient across the material [58]. The nanocomposite film demonstrates a high Seebeck coefficient value of − 0.26 V/K at room temperature compared to the neat resin film. The energy filtering effect on charge carriers enhances thermoelectric properties in organic–inorganic hybrid nanocomposites by establishing potential barriers between the polymer matrix and inorganic fillers [59]. This scattering of low-energy charge carriers increases the mean energy and Seebeck coefficient [59].

XPS analysis reveals multiple heterointerfaces between the resin matrix and GZO nanofillers, potentially strengthening the energy filtering effect and improving the thermoelectric properties of the nanocomposite film [60]. Park et al. suggest that heterointerfaces in polycrystalline nanocomposites, besides grain boundaries, can serve as phonon scattering sites, hindering thermal transport and

reducing electron–phonon interactions [61]. This further enhances carrier mobility and thermometric performance [61]. The power factor (PF) is highest for the nanocomposite film, reaching 261 nW/m·K^2 at room temperature, while it is negligible for the neat resin film, as indicated in Table 4. PF characterizes the performance of thermoelectric materials in thermal energy harvesting and conversion to electrical energy, calculated as follows [26]:

$$PF = \sigma S^2, \tag{4}$$

where σ is the electrical conductivity and S is the Seebeck coefficient. Enhancements in these properties result in higher PF and thermoelectric energy conversion efficiencies [26]. Thermoelectric properties are temperature-dependent, and wearable thermoelectric nanogenerators typically operate around room temperature [62].

Therefore, developing materials with good thermoelectric properties at room temperature is attractive for wearable thermoelectric energy harvesting applications (Video 1). For instance, Hu et al. produced an n-type Ni nanowires-PVDF nanocomposite film via the hydrothermal method, achieving a room-temperature PF of 11 nW/m·K^2 with 60wt% Ni nanofillers [63]. Hasan et al. developed a flexible thermoelectric nanogenerator for wearable applications, utilizing SWCNT films as the n-type thermoelements prepared through vacuum filtration and chemical treatment, yielding a room-temperature PF of 1.5 nW/m·K^2 [30]. Abd-Elsalam et al. developed an MWCNT/PANI nanocomposite film via chemical polymerization, showing a PF of 1.2 nW/m·K^2 near room temperature [64]. The developed n-type GZO-resin nanocomposite film holds promise for wearable thermoelectric nanogenerators, offering a high-power factor without sacrificing mechanical flexibility. It also comprises earth-abundant and non-toxic elements, is 3D printable, and offers cost-effectiveness and rapid prototyping advantages. These attributes position the photocurable GZO-resin nanocomposite film as an appealing option for expanding and commercializing wearable thermal energy harvesters.

Table 4 Thermoelectric properties of 3D-printed films at room temperature

Sample	Electrical conductivity (nS/m)	Seebeck coefficient (V/K)	Power factor (nW/m·K^2)
Photocurable resin	1026	0.0320	1.052
Photocurable resin-GZO nanocomposite	4001	− 0.255	260.8

3.5 Piezoelectric properties

The potential of 3D-printed films to generate electric current through mechanical deformations highlights their piezoelectric properties, as demonstrated

in Videos 2 and 3. Figure 8a, c illustrates the piezo-electric output voltages of resin and nanocomposite films in response to various mechanical deformation modes, such as constant tapping at 2.5N and bending at 90° [65–67]. Compared to the neat resin film, the nanocomposite film exhibits the highest output voltage response in both modes. This enhancement in piezoelectric properties is attributed to the hexagonal wurtzite crystal structure of GZO nanofillers, which possess a non-centrosymmetric structure, resulting in polar surfaces that enhance the piezoelectric properties of the 3D-printed nanocomposite film [24]. This is supported by the XRD pattern of the nanocomposite film, revealing crystalline diffraction peaks consistent with the ZnO wurtzite structure peaks. Additionally, XPS analysis indicates the presence of polar bonds (Zn–O and Ga–O), leading to the formation of electrically oppositely charged surfaces and molecular dipole moments [68].

Piezoelectric voltage polarity is positive and negative during mechanical deformation and release due to charge transport within piezoelectric materials

[66]. Figure 8b, d demonstrates the reorientation of dipole moments parallel to the direction of applied mechanical deformation on the nanocomposite film through the stress-induced poling effect, leading to net polarization and charge transport to the electrodes [68]. When the force is released, the material returns to its original shape, causing the dipoles to reorient randomly. This reverse deformation results in electrons flowing back through the external load (R) to the electrode, generating an electric signal in the opposite direction [67].

C-AFM analysis reveals multiphase constituents with dissimilar conductivity domains in the resin-GZO nanocomposite film. This may give rise to the Maxwell–Wagner–Sillars effect, accumulating mobile charges at the interface regions of nanofillers-matrix and creating interfacial polarization [31]. The uniform distribution of GZO nanofillers in the photocurable resin matrix, observed through SEM microstructure evolution, potentially enhances interfacial polarizations and piezoelectric performance. Furthermore, mechanical properties, particularly Young's modulus,
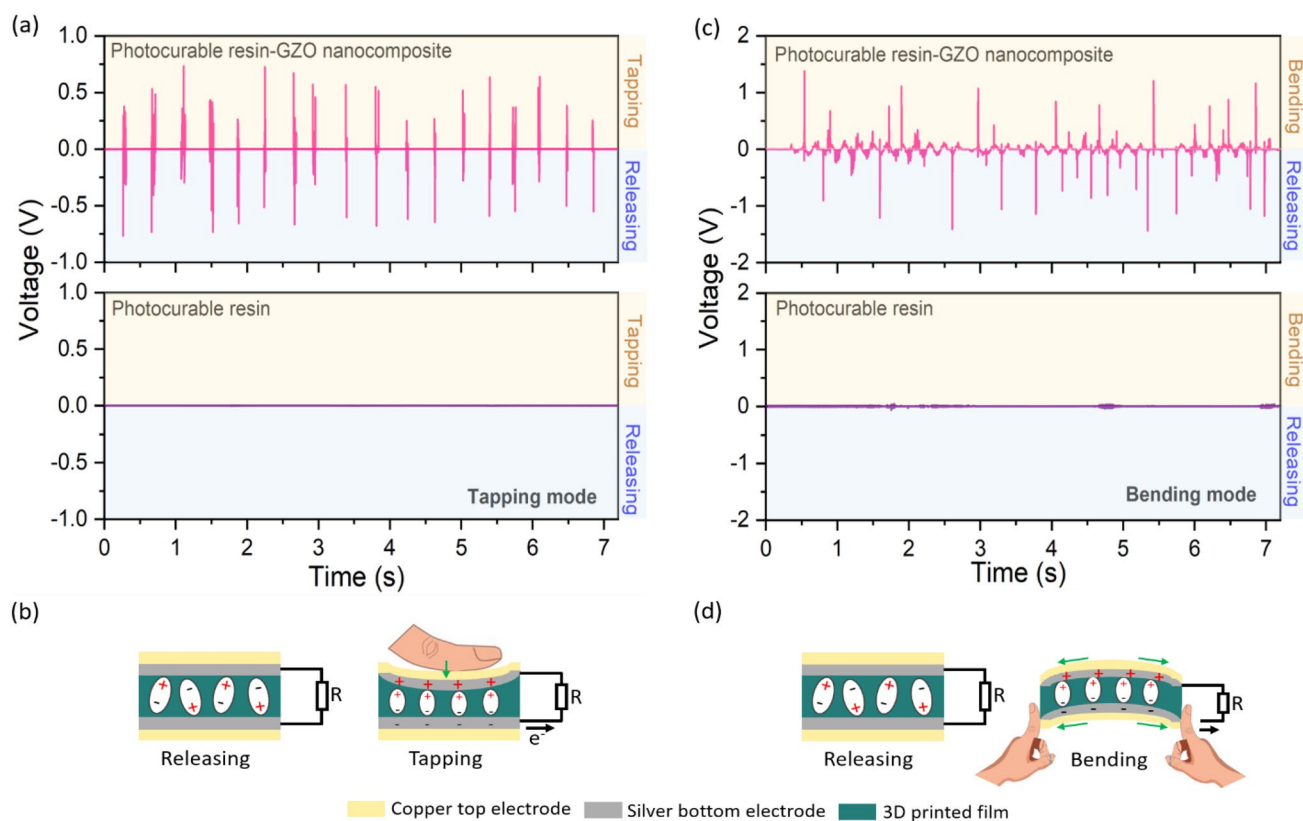

Fig. 8 Piezoelectric output voltages and mechanisms of 3D-printed films based on different mechanical deformation modes of **a**, **b** tapping and **c**, **d** bending

play a crucial role in the piezoelectric power generation of the nanocomposite film [69]. The nanocomposite film exhibits enhanced flexibility, as evidenced by its tailored stress–strain behavior.

Table 5 summarizes the peak-to-peak output voltages of 3D-printed films at room temperature. The nanocomposite film demonstrates the highest values, reaching 1.5 V and 2.8 V for tapping and bending movements, respectively. Notably, the bending mode yields nearly double the output voltage of tapping, suggesting that the nanocomposite film experiences maximum mechanical deformations under bending [39]. In this mode, the film experiences a bending stress that varies linearly along the length direction, resulting in a uniform and large strain distribution, making it a commonly used operation mode for piezoelectric nanogenerators [39]. The output current of resin and nanocomposite films under different modes is calculated considering a 3 MΩ load resistance to mimic the working conditions of piezoelectric harvesters [68]. High-output currents are observed from the piezoelectric energy conversion, with values of 940 nA and 498 nA for nanocomposite film under bending and tapping modes, respectively.

Instantaneous power density (P) calculated using Eq. (5) yields 592 nW/cm^2 and 207 nW/cm^2 from piezoelectric energy conversion across the nanocomposite film under bending and tapping deformations, respectively [54].

$$P = \frac{V^2}{RA},$$ (5)

where V is the output voltage, R is the load resistance, and A is the effective electrode area [53]. Zhou et al. developed a 3D-printed flexible piezoelectric nanogenerator based on BaTiO₃ nanoparticles and photocurable elastomers, achieving an output voltage of 0.29 V and power density of 57 nW/cm^2 upon stretching deformation [70]. García-Casas et al. demonstrated a power density of 20nW/cm^2 by finger tapping on flexible ZnO films fabricated by plasma technology on paper substrates for self-powering piezoelectric nanogenerators [71]. Wu et al. integrated solution-synthesized Se nanowires into wearable piezoelectric nanogenerators, showing a power density of 0.135 nW/cm^2 with bending movement [72]. The adequate power density, coupled with the mechanical flexibility of the developed photocurable resin-GZO nanocomposite film derived from earth-abundant elements and cost-effective technology, presents an attractive prospect for flexible piezoelectric nanogenerators, sensors, or hybrid wearable energy harvesters.

4 Conclusions

This study integrates additive manufacturing through 3D printing technology with Ga-doped ZnO (GZO), an abundant and non-toxic material, to enhance energy sustainability and improve market competitiveness in wearable thermoelectric and piezoelectric devices. A comprehensive set of analyses, including thermal, structural, mechanical, thermoelectric, and piezoelectric measurements on 3D-printed films of the photocurable resin-GZO nanocomposite, has provided valuable insights into their energy harvesting capabilities. TGA analysis confirmed the nanocomposite film's thermal stability within a range suitable for wearable energy harvesters. XRD analysis revealed a distinct crystalline structure compared to the amorphous neat resin film, indicating the successful integration of GZO nanofillers. SEM–EDS showcased a bulk-like microstructure with uniformly distributed GZO nanofillers. XPS analysis confirmed the composite nature of the film, associating core levels with GZO nanofillers and the resin matrix. Additionally, C-AFM analysis unveiled a fine granular structure and conductive domains within the nanocomposite film, attributed to the dispersion of nano-sized GZO particles. The presence of GZO nanofillers tailored the stress–strain

Table 5 Piezoelectric properties of 3D-printed films at room temperature

Sample	Tapping mode			Bending mode		
	Voltage (V)	Current (nA)	Power density (nW/cm^2)	Voltage (V)	Current (nA)	Power density (nW/cm^2)
Photocurable resin	0.00397	1.32	0.00195	0.0560	18.7	0.387
Photocurable resin-GZO nanocomposite	1.50	498	207	2.82	940	592

behavior, leading to enhancements in the flexibility of the nanocomposite film. Notably, the nanocomposite film exhibited substantially higher power factors and piezoelectric power densities than the neat resin film. Combined with its mechanical flexibility and cost-effective production, these attributes position it as an attractive approach for flexible thermoelectric and piezoelectric nanogenerators and hybrid wearable energy harvesters. Continued research and development of GZO films are essential to fully realize their potential and address existing challenges in thermoelectric and piezoelectric energy harvesting applications. This includes exploring the piezoelectric stress profile within GZO films during mechanical deformations to enhance their performance further.

Author contributions

Aicha S. Lemine: Conceptualization, Methodology, Data curation, and Writing—original draft. Jolly Bhadra: Validation, Supervision, and Writing—review and editing. Kishor Kumar Sadasivuni: Validation, Supervision, and Writing—review and editing. Anton Popelka: Data resource and Writing—review and editing. Swathi Yempally: Data resource. Zubair Ahmad: Writing—review and editing. Noora J. Al-Thani: Writing—review and editing. Anwarul Hasan: Validation, Supervision, and Writing—review and editing. All authors have read and agreed to the published version of the manuscript.

Data availability

The authors declare that the data that support the findings of this study are available on request from the corresponding author.

Declarations

Competing interest The authors declare that they have no known competing financial interests or personal relationships that could have appeared to influence the work reported in this paper.

Supplementary Information The online version contains supplementary material available at https://doi.org/10.1007/s10854-024-13372-z.

References

1. A. Ali, H. Shaukat, S. Bibi, W.A. Altabey, M. Noori, S.A. Kouritem, Recent progress in energy harvesting systems for wearable technology. Energy Strateg. Rev. **49**, 101124 (2023). https://doi.org/10.1016/j.esr.2023.101124

2. S. Uhl, M. Pellet, J. Tschanz, E. Laux, T. Journot, L. Jeandupeux et al., Fabrication of highly-integrated thermoelectric generators based on ionic liquids. Mater. Today Proc. **2**, 669–674 (2015). https://doi.org/10.1016/j.matpr.2015.05.084

3. N. Ben Saber, A. Mezni, A. Alrooqi, T. Altalhi, A review of ternary nanostructures based noble metal/semiconductor for environmental and renewable energy applications. J. Mater. Res. Technol. **9**, 15233–15262 (2020). https://doi.org/10.1016/j.jmrt.2020.10.090

4. Z. Fan, Y. Zhang, L. Pan, J. Ouyang, Q. Zhang, Recent developments in flexible thermoelectrics: from materials to devices. Renew. Sustain. Energy Rev. **137**, 110448 (2021). https://doi.org/10.1016/j.rser.2020.110448

5. J. Zhang, Y. He, C. Boyer, K. Kalantar-Zadeh, S. Peng, D. Chu et al., Recent developments of hybrid piezo-triboelectric nanogenerators for flexible sensors and energy harvesters. Nanoscale Adv. **3**, 5465–5486 (2021). https://doi.org/10.1039/d1na00501d

6. A. Megdich, M. Habibi, L. Laperrière, A review on 3D printed piezoelectric energy harvesters: materials, 3D printing techniques, and applications. Mater. Today Commun. (2023). https://doi.org/10.1016/j.mtcomm.2023.105541

7. A.S. Lemine, O. Fayyaz, R.A. Shakoor, Z. Ahmad, J. Bhadra, N.J. Al-Thani, Effect of cold and hot compactions on corrosion behavior of p-and n-type bismuth telluride-based alloys developed through microwave sintering process. J. Alloys Compd. **939**, 168763 (2023). https://doi.org/10.1016/j.jallcom.2023.168763

8. Han, S. W., Hasan, M. D., Kim, J. Y., Lee, H. W., Lee, K. H., & Kim OJ. Multi-physics analysis for the design and development of micro-thermoelectric coolers. Proc Soc Control Robot Syst Conf 2005 pp. 139–44

9. P. Wu, Z. He, M. Yang, J. Xu, N. Li, Z. Wang et al., A review on flexible thermoelectric technology: material, device, and applications. Int. J. Thermophys. (2021). https://doi.org/10.1007/s10765-021-02860-7

10. S. Abubakar, N. Khalid, S.F. Abd Rahman, T.S. Tee, M.N. Hamidon, Z.A. Talib et al., Fabrication and characterization of nanostructured zinc oxide on printed microcontact electrode for piezoelectric applications. J. Mater. Res. Technol. **9**, 15952–15961 (2020). https://doi.org/10.1016/j.jmrt.2020.11.038

11. S. Kumar, H.H. Singh, N. Khare, Flexible hybrid piezoelectric-thermoelectric generator for harnessing electrical energy from mechanical and thermal energy. Energy Convers. Manag. **198**, 111783 (2019). https://doi.org/10.1016/j.enconman.2019.111783

12. M.E. Kiziroglou, E.M. Yeatman, Materials and techniques for energy harvesting. Funct. Mater. Sustain. Energy Appl. (2012). https://doi.org/10.1533/9780857096371.4.539

13. Y. Bozkurt, E. Karayel, 3D printing technology; methods, biomedical applications, future opportunities and trends. J. Mater. Res. Technol. **14**, 1430–1450 (2021). https://doi.org/10.1016/j.jmrt.2021.07.050

14. A. Cortés, M. Bañón-Veracruz, A. Jiménez-Suárez, M. Campo, M.G. Prolongo, S.G. Prolongo, Enhancing efficiency and sustainability of digital light processing 3D-Printing by novel two-stage processing of carbon nanotube reinforced nanocomposites. J. Mater. Res. Technol. **29**, 3237–3248 (2024). https://doi.org/10.1016/j.jmrt.2024.02.018

15. B. Berman, 3-D printing: the new industrial revolution. Bus. Horiz. **55**, 155–162 (2012). https://doi.org/10.1016/j.bushor.2011.11.003

16. I. Roohani, A. Entezari, H. Zreiqat, Liquid crystal display technique (LCD) for high resolution 3D printing of tri-ply periodic minimal surface lattices bioceramics. Addit. Manuf. **74**, 103720 (2023). https://doi.org/10.1016/j.addma.2023.103720

17. A. Al Rashid, S.A. Khan, G. Al-Ghamdi S, Koç M, Additive manufacturing of polymer nanocomposites: needs and challenges in materials, processes, and applications. J. Mater. Res. Technol. **14**, 910–941 (2021). https://doi.org/10.1016/j.jmrt.2021.07.016

18. F. Kim, B. Kwon, Y. Eom, J.E. Lee, S. Park, S. Jo et al., 3D printing of shape-conformable thermoelectric materials using all-inorganic Bi_2Te_3-based inks. Nat. Energy **3**, 301–309 (2018). https://doi.org/10.1038/s41560-017-0071-2

19. M. He, Y. Zhao, B. Wang, Q. Xi, J. Zhou, Z. Liang, 3D printing fabrication of amorphous thermoelectric materials with ultralow thermal conductivity. Small **11**, 5889–5894 (2015). https://doi.org/10.1002/smll.201502153

20. D. Park, S. Lee, J. Kim, Enhanced thermoelectric performance of UV-curable silver (I) selenide-based composite for energy harvesting. Sci. Rep. **11**, 1–8 (2021). https://doi.org/10.1038/s41598-021-96267-x

21. X. Zhou, K. Parida, O. Halevi, Y. Liu, J. Xiong, S. Magdassi et al., All 3D-printed stretchable piezoelectric nanogenerator with non-protruding kirigami structure. Nano Energy **72**, 104676 (2020). https://doi.org/10.1016/j.nanoen.2020.104676

22. K. Kim, W. Zhu, X. Qu, C. Aaronson, W.R. McCall, S. Chen et al., 3D optical printing of piezoelectric nanoparticle-polymer composite materials. ACS Nano **8**, 9799–9806 (2014). https://doi.org/10.1021/nn503268f

23. T. Varghese, C. Hollar, J. Richardson, N. Kempf, C. Han, P. Gamarachchi et al., High-performance and flexible thermoelectric films by screen printing solution-processed nanoplate crystals. Sci. Rep. **6**, 6–11 (2016). https://doi.org/10.1038/srep33135

24. N. Bhadwal, R. Ben Mrad, K. Behdinan, Review of zinc oxide piezoelectric nanogenerators: piezoelectric properties composite structure power output. Sensors (2023). https://doi.org/10.3390/s23083859

25. M. Aleksandrova, Polymeric seed layer as a simple approach for nanostructuring of Ga-doped ZnO films for flexible piezoelectric energy harvesting. Microelectron. Eng. **233**, 111434 (2020). https://doi.org/10.1016/j.mee.2020.111434

26. A.S. Lemine, J. Bhadra, N.J. Al-Thani, Z. Ahmad, Promising transparent and flexible thermoelectric modules based on p-type CuI thin films—A review. Energy Rep. **8**, 11607–11637 (2022). https://doi.org/10.1016/j.egyr.2022.09.020

27. V. Pandiyarasan, S. Suhasini, J. Archana, M. Navaneethan, A. Majumdar, Y. Hayakawa et al., Fabrication of hierarchical ZnO nanostructures on cotton fabric for wearable device applications. Appl. Surf. Sci. **418**, 352–361 (2017). https://doi.org/10.1016/j.apsusc.2016.12.202

28. A. Mahapatra, R.S. Ajimsha, M.O. Ittoop, A. Sharma, S. Karmakar, A. Shaikh et al., Flexible ZnO:PVDF based free standing piezoelectric nanogenerator for vibrational energy harvesting and wearable shoe insole pedometer sensor. J. Alloys Compd. **960**, 170898 (2023). https://doi.org/10.1016/j.jallcom.2023.170898

29. F.E. Jorge, L.G.P. Tienne, M.D.F.V. Marques, S.N. Monteiro, Evaluation of thermoelectric properties of hybrid polyaniline nanocomposites incorporated with graphene oxide and zinc oxide with different morphologies. J. Mater. Res. Technol. **27**, 6822–6832 (2023). https://doi.org/10.1016/j.jmrt.2023.11.098

30. M.N. Hasan, M.I. Ahmad Asri, T. Saleh, A.G.A. Muthalif, M.S. Mohamed Ali, Wearable thermoelectric generator with vertically aligned PEDOT:PSS and carbon nanotubes thermoelements for energy harvesting. Int. J. Energy Res. **46**, 15824–15836 (2022). https://doi.org/10.1002/er.8283

31. H. Parangusan, D. Ponnamma, M.A.A. Al-Maadeed, Stretchable electrospun PVDF-HFP/Co-ZnO nanofibers as piezoelectric nanogenerators. Sci. Rep. **8**, 1–11 (2018). https://doi.org/10.1038/s41598-017-19082-3

32. K. Skorenko, R.T. Bernier, J. Liu, B. Galusha, F. Goroleski, B.P. Hughes et al., Thermal stability of ZnO nanoparticle bound organic chromophores. Dye. Pigment. **131**, 69–75 (2016). https://doi.org/10.1016/j.dyepig.2016.03.011

33. Y. Shmueli, G.E. Shter, O. Assad, H. Haick, P. Sonntag, P. Ricoux et al., Structural and electrical properties of single Ga/ZnO nanofibers synthesized by electrospinning. J. Mater. Res. **27**, 1672–1679 (2012). https://doi.org/10.1557/jmr.2012.118

34. A.A. El Bellihi, W.A. Bayoumy, E.M. Masoud, M.A. Mousa, Preparation, characterizations and conductivity of composite polymer electrolytes based on PEO-LiClO4 and nano ZnO filler. Bull. Korean Chem. Soc. **33**, 2949–2954 (2012). https://doi.org/10.5012/bkcs.2012.33.9.2949

35. V. Jančovičová, M. Mikula, B. Havlínová, Z. Jakubíková, Influence of UV-curing conditions on polymerization kinetics and gloss of urethane acrylate coatings. Prog. Org. Coatings **76**, 432–438 (2013). https://doi.org/10.1016/j.porgcoat.2012.10.010

36. J. Zhao, Q. Li, F. Jin, N. He, Digital light processing 3D printing Kevlar composites based on dual curing resin. Addit. Manuf. **41**, 101962 (2021). https://doi.org/10.1016/j.addma.2021.101962

37. A.K. Zak, W.A. Majid, M.E. Abrishami, R. Yousefi, X-ray analysis of ZnO nanoparticles by Williamson-Hall and size-strain plot methods. Solid State Sci. **13**, 251–256 (2011). https://doi.org/10.1016/j.solidstatesciences.2010.11.024

38. X. Chen, H.O.T. Ware, E. Baker, W. Chu, J. Hu, C. Sun, The development of an all-polymer-based piezoelectric photocurable resin for additive manufacturing. Procedia CIRP **65**, 157–162 (2017). https://doi.org/10.1016/j.procir.2017.04.025

39. M.S. Sorayani Bafqi, A.H. Sadeghi, M. Latifi, R. Bagherzadeh, Design and fabrication of a piezoelectric out-put evaluation system for sensitivity measurements of fibrous sensors and actuators. J. Ind. Text. **50**, 1643–1659 (2021). https://doi.org/10.1177/1528083719867443

40. D.H. Cho, J.H. Kim, B.M. Moon, Y.D. Jo, S.M. Koo, Control of a- and c-plane preferential orientations of ZnO thin films. Appl. Surf. Sci. **255**, 3480–3484 (2009). https://doi.org/10.1016/j.apsusc.2008.09.073

41. A.S. Lemine, O. Fayyaz, M. Yusuf, R.A. Shakoor, Z. Ahmad, J. Bhadra et al., Microstructure and mechanical properties of aluminum matrix composites with bimodal-sized hybrid NbC-B4C reinforcements. Mater Today Commun. **33**, 104512 (2022). https://doi.org/10.1016/j.mtcomm.2022.104512

42. Vu.D. Viet, D. Le Hai, C. Xuan Nguyen, T.T. Quang, Comparison of structural and electric properties of ZnO-based n-type thin films with different dopants for thermoelectric

applications. J. Sol-Gel Sci. Technol. **91**, 146–153 (2019). https://doi.org/10.1007/s10971-019-05024-0

43. J. Jancar, J.F. Douglas, F.W. Starr, S.K. Kumar, P. Cassagnau, A.J. Lesser et al., Current issues in research on structure-property relationships in polymer nanocomposites. Polymer (Guildf) **51**, 3321–3343 (2010). https://doi.org/10.1016/j.polymer.2010.04.074

44. V.V.P. Munaga, T. Krishnan, R.K. Borra, Structural, surface morphological, optical and thermoelectric properties of sol–gel spin coated Zn doped CdS thin films. SN Appl. Sci. **2**, 1–12 (2020). https://doi.org/10.1007/s42452-020-2358-3

45. T. Prasada Rao, M.C. Santhosh Kumar, Physical properties of Ga-doped ZnO thin films by spray pyrolysis. J. Alloys Compd. **506**, 788–793 (2010). https://doi.org/10.1016/j.jallcom.2010.07.071

46. H. Ennaceri, M. Boujnah, D. Erfurt, J. Rappich, X. Lifei, A. Khaldoun et al., Influence of stress on the photocatalytic properties of sprayed ZnO thin films. Sol. Energy Mater. Sol. Cells (2019). https://doi.org/10.1016/j.solmat.2019.110058

47. G. Atanasova, A.O. Dikovska, M. Stankova, P. Stefanov, P.A. Atanasov, XPS study of ZnO nanostructures prepared by laser ablation. J. Phys. Conf. Ser. (2012). https://doi.org/10.1088/1742-6596/356/1/012036

48. Z. Xu, K. Tang, S. Zhu, J. Ma, J. Ye, S. Gu, Identification and tuning of zinc-site nitrogen-related complexes in ZnO material. J. Vac. Sci. Technol. A Vac. Surf. Film (2018). https://doi.org/10.1116/1.4996617

49. S.H. Ji, W. Lee, J.S. Yun, All-in-one piezo-triboelectric energy harvester module based on piezoceramic nanofibers for wearable devices. ACS Appl. Mater. Interfaces **12**, 18609–18616 (2020). https://doi.org/10.1021/acsami.0c02754

50. X. Wang, A. Lamantia, M. Jay, H. Sadeghi, C.J. Lambert, O.V. Kolosov et al., Determination of electric and thermoelectric properties of molecular junctions by AFM in peak force tapping mode. Nanotechnology (2023). https://doi.org/10.1088/1361-6528/acdf67

51. H.I. Yang, K.R. Naveen, S.M. Cho, J.Y. Kim, Y.H. Jung, J.H. Kwon, Systematic investigation on polymer layer selection for flexible thin film encapsulation. Org. Electron. **115**, 106761 (2023). https://doi.org/10.1016/j.orgel.2023.106761

52. B. van Bochove, D.W. Grijpma, Mechanical properties of porous photo-crosslinked poly(trimethylene carbonate) network films. Eur. Polym. J. **143**, 110223 (2021). https://doi.org/10.1016/j.eurpolymj.2020.110223

53. H. Shang, C. Dun, Y. Deng, T. Li, Z. Gao, L. Xiao et al., Bi0.5Sb1.5Te3-based films for flexible thermoelectric

devices. J. Mater. Chem. A **8**, 4552–4561 (2020). https://doi.org/10.1039/c9ta13152c

54. H. Parangusan, D. Ponnamma, M.A.A. Almaadeed, Investigation on the effect of γ-irradiation on the dielectric and piezoelectric properties of stretchable PVDF/Fe-ZnO nanocomposites for self-powering devices. Soft Matter **14**, 8803–8813 (2018). https://doi.org/10.1039/c8sm01655k

55. Y. Na, S. Kim, S.P.R. Mallem, S. Yi, K.T. Kim, P. Kl, Energy harvesting from human body heat using highly flexible thermoelectric generator based on Bi2Te3 particles and polymer composite. J. Alloys Compd. **924**, 166575 (2022). https://doi.org/10.1016/j.jallcom.2022.166575

56. A.S. Lemine, F.M. El-Makaty, H.A. Al-Ghanim, K.M. Youssef, Experimental and modeling analysis of p-type Bi0.4Sb1.6Te3 and graphene nanocomposites. J. Mater. Res. Technol. **16**, 1702–1712 (2022). https://doi.org/10.1016/j.jmrt.2021.12.096

57. A. Mehdizadeh Dehkordi, M. Zebarjadi, J. He, T.M. Tritt, Thermoelectric power factor: enhancement mechanisms and strategies for higher performance thermoelectric materials. Mater. Sci. Eng. R. Rep. **97**, 1–22 (2015). https://doi.org/10.1016/j.mser.2015.08.001

58. H. Ju, J. Kim, Preparation and structure dependent thermoelectric properties of nanostructured bulk bismuth telluride with graphene. J. Alloys Compd. **664**, 639–647 (2016). https://doi.org/10.1016/j.jallcom.2016.01.002

59. Q. Zhang, X. Ai, L. Wang, Y. Chang, W. Luo, W. Jiang et al., Improved thermoelectric performance of silver nanoparticles-dispersed Bi2Te3composites deriving from hierarchical two-phased heterostructure. Adv. Funct. Mater. **25**, 966–976 (2015). https://doi.org/10.1002/adfm.201402663

60. A. Soni, Y. Shen, M. Yin, Y. Zhao, L. Yu, X. Hu et al., Interface driven energy filtering of thermoelectric power in spark plasma sintered Bi2Te 2.7Se 0.3 nanoplatelet composites. Nano Lett. **12**, 4305–4310 (2012). https://doi.org/10.1021/nl302017w

61. D. Park, S. Lee, J. Kim, Thermoelectric and mechanical properties of PEDOT:PSS-coated Ag2Se nanowire composite fabricated via digital light processing based 3D printing. Compos. Commun. **30**, 101084 (2022). https://doi.org/10.1016/j.coco.2022.101084

62. W. Liu, H.S. Kim, Q. Jie, Z. Ren, Importance of high power factor in thermoelectric materials for power generation application: a perspective. Scr. Mater. **111**, 3–9 (2016). https://doi.org/10.1016/j.scriptamat.2015.07.045

63. S. Hu, S. Zeng, X. Li, J. Jiang, W. Yang, Y. Chen et al., Flexible and high performance of n-type thermoelectric PVDF composite film induced by nickel nanowires. Mater.

Des. **188**, 108496 (2020). https://doi.org/10.1016/j.matdes.2020.108496

64. A. Abd-Elsalam, H.O. Badr, A.A. Abdel-Rehim, I.S. El-Mahallawi, Structure and thermoelectric behavior of polyaniline-based/ CNT-composite. Curr. Appl. Phys. **36**, 88–92 (2022). https://doi.org/10.1016/j.cap.2021.11.012

65. H. Parangusan, K. Karuppasamy, J. Bhadra, Tailored nanofiber composites for a flexible piezoelectric nanogenerator: Poly(vinylidene fluoride) with BaTiO3/NiFe2O4. J. Alloys Compd. **989**, 174254 (2024). https://doi.org/10.1016/j.jallcom.2024.174254

66. A. Khorsand Zak, S.T. Yazdi, M.E. Abrishami, A.M. Hashim, A review on piezoelectric ceramics and nanostructures: fundamentals and fabrications. J. Aust. Ceram. Soc. **60**, 723–753 (2024). https://doi.org/10.1007/s41779-024-00990-3

67. M. Misra, A.K. Srivastava, A.N. Kadam, T.T. Salunkhe, V. Kumar, A.P.G. Nikalje, Substantial enhancement of optoelectronics and piezoelectric properties of novel hollow ZnO nanorods towards efficient flexible touch and bending sensor. Coll. Surf. A Physicochem. Eng. Asp **685**, 133232 (2024). https://doi.org/10.1016/j.colsurfa.2024.133232

68. H. Kaczmarek, B. Królikowski, E. Klimiec, J. Kowalonek, New piezoelectric composites based on isotactic polypropylene filled with silicate. J. Mater. Sci. Mater. Electron. **28**, 6435–6447 (2017). https://doi.org/10.1007/s10854-016-6329-9

69. X. Zhou, K. Parida, J. Chen, J. Xiong, Z. Zhou, F. Jiang et al., 3D printed auxetic structure-assisted piezoelectric energy harvesting and sensing. Adv. Energy Mater. **13**, 1–10 (2023). https://doi.org/10.1002/aenm.202301159

70. X. Zhou, K. Parida, O. Halevi, S. Magdassi, All 3D printed stretchable piezoelectric nanogenerator for self-powered sensor application. Sensors **23**, 6748 (2020). https://doi.org/10.3390/s20236748

71. X. García-Casas, F.J. Aparicio, J. Budagosky, A. Ghaffarinejad, N. Orozco-Corrales, K.K. Ostrikov et al., Paper-based ZnO self-powered sensors and nanogenerators by plasma technology. Nano Energy (2023). https://doi.org/10.1016/j.nanoen.2023.108686

72. M. Wu, Y. Wang, S. Gao, R. Wang, C. Ma, Z. Tang et al., Solution-synthesized chiral piezoelectric selenium nanowires for wearable self-powered human-integrated monitoring. Nano Energy **56**, 693–699 (2019). https://doi.org/10.1016/j.nanoen.2018.12.003